





# Analytical database of Martian minerals (ADaMM): Project synopsis and Raman data overview

Marco Veneranda<sup>1</sup>  | Aurelio Sanz-Arranz<sup>1</sup> | Jose Antonio Manrique<sup>1</sup> |  
Jesus Saiz<sup>1</sup> | Clara Garcia-Prieto<sup>1</sup> | Elena Pascual-Sánchez<sup>1</sup> | Jesus Medina<sup>1</sup> |  
Menelaos Konstantinidis<sup>2</sup> | Emmanuel Lalla<sup>2</sup>  | Andoni Moral<sup>3</sup>  |  
Luis Miguel Nieto<sup>1</sup> | Fernando Rull<sup>1</sup> | Guillermo Lopez-Reyes<sup>1</sup> 

<sup>1</sup>Universidad de Valladolid, Valladolid, Spain

<sup>2</sup>York University, Toronto, Canada

<sup>3</sup>Instituto Nacional de Técnica Aeroespacial (INTA), Madrid, Spain

## Correspondence

Marco Veneranda, Universidad de Valladolid, Ave. Francisco Vallés, 8, 47151, Valladolid, Spain.  
Email: marco.veneranda.87@gmail.com

## Funding information

H2020 European Research Council, Grant/Award Number: 687302; Ministry of Economy and Competitiveness, Grant/Award Number: PID2019-107442RB-C31

## Abstract

The Mars2020/Perseverance and ExoMars/Rosalind Franklin rovers are both slated to return the first Raman spectra ever collected from another planetary surface, Mars. In order to optimize the rovers scientific outcome, the scientific community needs to be provided with tailored tools for data treatment and interpretation. Responding to this need, the purpose of the Analytical Database of Martian Minerals (ADaMM) project is to build an extended multianalytical database of mineral phases that have been detected on Mars or are expected to be found at the landing sites where the two rovers will operate. Besides the use of conventional spectrometers, the main objective of the ADaMM database is to provide access to data collected by means of laboratory prototypes simulating the analytical performances of the spectroscopic systems onboard the Mars 2020 and ExoMars rovers. Planned to be released to the public in 2022, ADaMM will also provide access to data treatment and visualization tools developed in the framework of the mentioned space exploration missions. As such, the present work seeks to provide an overview of the ADaMM online platform, spectral tools, and mineral collection. In addition to that, the manuscript describes the Raman spectrometers used to analyze the mineral collection and presents a representative example of the analytical performance ensured by the Raman prototypes assembled to simulate the Raman Laser Spectrometer (RLS) and SuperCam systems.

## KEYWORDS

ExoMars, Mars 2020, mineral database, Raman, spectroscopy

This is an open access article under the terms of the Creative Commons Attribution-NonCommercial-NoDerivs License, which permits use and distribution in any medium, provided the original work is properly cited, the use is non-commercial and no modifications or adaptations are made.

© 2021 The Authors. *Journal of Raman Spectroscopy* published by John Wiley & Sons Ltd.

## 1 | INTRODUCTION

Beyond remote sensing analyses, surface spectroscopy techniques are acquiring an increasing importance in the in situ investigation of celestial bodies. Focusing on Mars, the Mars 2020/Perseverance rover landed at Jezero Crater in February 2021 to perform in situ analytical investigations and to collect and store astrobiologically relevant samples to be collected and stored for a future Sample Return Mission [1, 2]. To do so, the analysis of geological targets is entrusted to the geochemical and mineralogical data collected by a set of remote and proximity spectroscopic systems. In detail, the SuperCam instrument investigates the chemical and mineral makeup composition of remote samples through a combination of complementary Laser Induced Breakdown Spectroscopy (LIBS), Raman, Vis-IR, and fluorescence analysis [3, 4]. Once a target of high scientific interest is selected, additional spectroscopic analyses are eventually performed by Planetary Instrument for X-ray Lithochemistry (PIXL, a X-Ray fluorescence spectrometer [5]) and SHERLOC (Deep UV-Raman and fluorescence spectrometer [6]), two payload instruments coupled to the robotic arm of the rover.

Scheduled to be launched in 2022, the ESA-ROSCOSMOS/ExoMars mission will deploy the Rosalind Franklin rover at Oxia Planum to address the question of whether life has ever existed on Mars [7]. To achieve this goal, the analytical laboratory of the rover is equipped with MOMA (Mars Organic Molecule Analyzer [8]), a mass spectrometer-based instrument developed to detect minor traces of organic molecules potentially preserved within the geological matrix of subsurface samples collected by a drill from a depth of up to 2 m. As the instrument will allow a limited number of analyses, the selection of astrobiologically relevant samples to be analyzed by MOMA is entrusted to the combined use of MicrOmega [9] (VNIR spectrometer) and Raman Laser Spectrometer [10] (RLS) systems.

Besides the analytical systems onboard Mars 2020 and ExoMars rovers, further spectroscopic systems are being developed for planetary missions to come. For example, the Martian Moons eXploration (MMX) rover [11], which the Japan Aerospace Exploration Agency (JAXA) is planning to land on Phobos in 2024 [11], will be equipped with the RAX spectrometer (Raman spectrometer for MMX, partially derived from the ExoMars/RLS) [12]. Raman spectroscopy has been also identified as one of the analytical techniques necessary to meet the science goals outlined for the NASA/Europa Lander mission concept [13], and dedicated Raman prototypes are under development [14, 15].

Considering that the increasing weight spectroscopic techniques (especially Raman) are acquiring in the field of

planetary exploration, the scientific community needs to be provided with the necessary tools to maximize the scientific exploitation of the retrieved data. Responding to this need, the PTAL (Planetary Terrestrial Analogs Library) project aims to provide the scientific community with a multi-analytical database of terrestrial analog materials studied by planetary mission instrumentation [16–18]. Similar to terrestrial analog collections (as PTAL), spectroscopic databases of pure mineral patterns are an essential tool to analyze the spectra returned from planetary missions. Even though many mineral databases are nowadays available [19–22], their usefulness is limited when interpreting spectra from space. Indeed, a reliable comparison of the detected spectroscopic features cannot be truly performed, as reference spectra are mostly collected through state-of-the-art spectroscopic systems whose analytical performances are not comparable to those from the instrumentation developed for space exploration missions. To overcome this limitation, the ADaMM (Analytical Database of Martian Minerals) project aims to support Mars 2020 and ExoMars missions by providing the scientific community with the first analytical database including spectra qualitatively comparable to those provided by the spectrometers onboard the Perseverance and Rosalind Franklin rovers [23]. In detail, knowing that several members of this project are directly involved in the development of the SuperCam and RLS systems, ADaMM samples have been analyzed using analytical prototypes that emulate the analytical performances of the two flight models.

In this light, the present work provides a general overview of the ADaMM online platform, the spectroscopic tools accessible through the website and the mineral collection composing the database. Furthermore, focusing on Raman data, this manuscript also describes the Raman spectrometers used for ADaMM samples characterization and provides a representative example of the role that Raman data gathered by prototypes simulating RLS and SuperCam can play in optimizing the interpretation of the Raman spectra returned from Mars.

## 2 | ADaMM ONLINE PLATFORM

Once the development of the ADaMM online platform is completed, a dedicated manuscript will be presented. However, the main characteristics of the platform design are summarized below.

### 2.1 | Database design

Inheriting the online platform developed in the framework of the PTAL project, the ADaMM database system

is mounted as described in Figure 1, using PostgreSQL for the database management, an Apache server, and a dynamic html interface generated using Django for web access. Django also manages the user access credentials and permissions.

The database follows a sample-centered design, linking the samples to their corresponding analyses, instruments, and results. In this way, it will be possible to navigate the database while keeping the traceability of the results with the corresponding sample, analysis, instrument, and technique, allowing a user-friendly environment to browse through all the information related to a determined sample.

## 2.2 | Database management

The Database management (adding, editing, or removing data from the database) can be performed only through the web interface, but this activity is only in principle foreseen for the database administrators. On the other hand, the database user will be able to access the data for visualization and download through a web browser and also by means of a dedicated software known as SpectPro (see Section 3). Access to the database will require a login account with a password.

## 2.3 | Sample browsing

By clicking on the dedicated icon, the list of available mineral samples will be provided. It will be possible to search for a determined result by querying by any of the fields shown in the table (name, parent sample, preparation, campaign, etc.). Additional details about the sample will be also displayed together with the associated diffractometric and spectroscopic data.

## 2.4 | Analyses summary

Each sample allows accessing a summary of all its related analyses and results. It is possible to navigate to this information simply by clicking on the Analyses Summary link in the sample browsing view. The overlaid information shows a summary of the results found for the sample, providing also access to analytical details by clicking on the corresponding analysis on the green box.

## 2.5 | Analysis details

By selecting a specific analysis, the ADaMM database will provide the related details (acquisition parameters, date of analysis, data interpretation, etc.). All the analytical

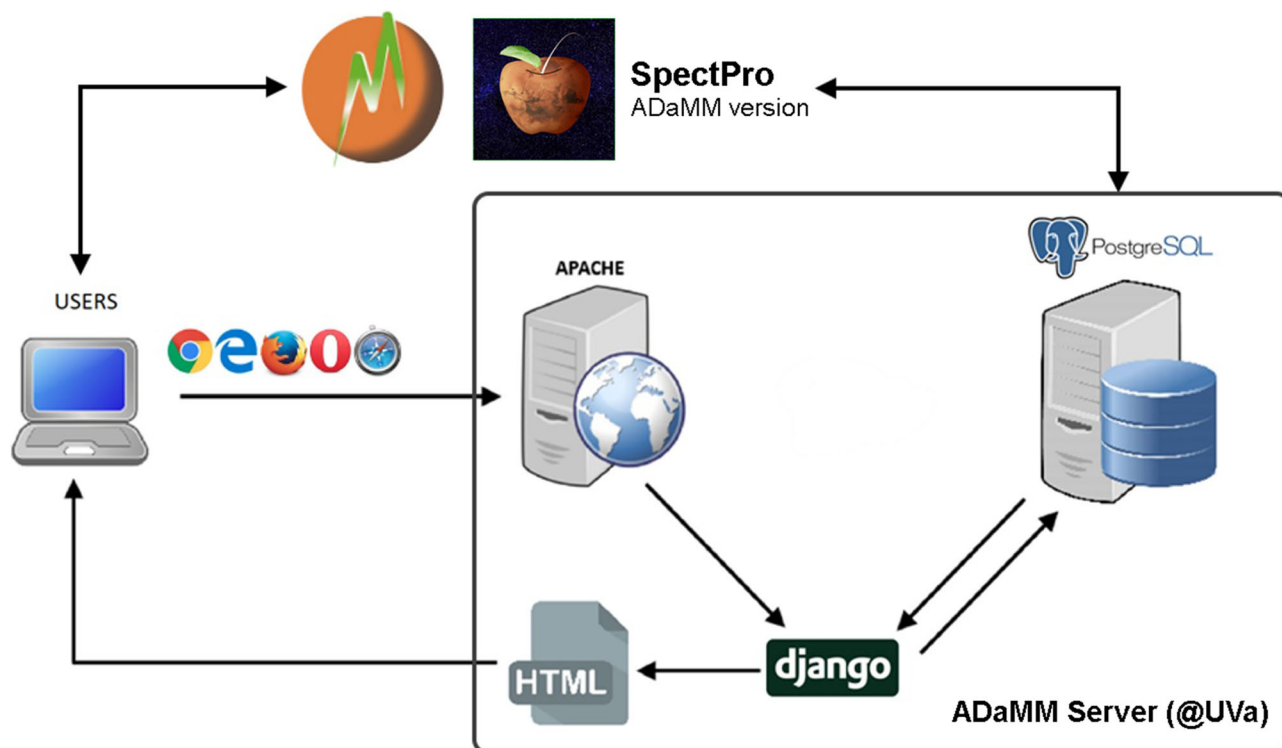


FIGURE 1 Analytical Database of Martian Minerals (ADaMM) server design [Colour figure can be viewed at wileyonlinelibrary.com]

data can be either previewed in the explorer or downloaded. By the end of the project, this feature will be available for both Microsoft and MacOS operating systems.

### 3 | SPECTPRO SOFTWARE

The Instrument Data Analysis Tool (IDAT)/SpectPro software was developed by the University of Valladolid to receive, decode, calibrate, and verify the telemetry information generated by the RLS instrument on Mars [10, 23, 24]. IDAT/SpectPro also provides access to an extended set of analytical tools for spectral analysis and features a general-purpose spectrum calculator.

In the framework of the ADaMM project, a tailored version of the IDAT/SpectPro software was created and coupled to the mineral database to be used for data visualization and treatment. The SpectPro installer can be downloaded by authorized users from the ADaMM online platform, and after installation, the login can be performed by using the same credentials as for the ADaMM database. The software is directly connected to the ADaMM platform, so that spectroscopic data can be automatically retrieved from the database (using dedicated searching tools) and displayed in the SpectPro interface.

As displayed in Figure 2, the main display is organized in four different panels:

- The central panel is where the spectrum is represented.
- The session data panel shows two tabs with all the spectra and operations performed in the current session (including all windows). The lower part of the panel shows the information of the selected element.
- The Session window shows the spectra and operations performed on the active window. Clicking a spectrum brings it to the front. The lower part of the panel shows the information of the selected element.
- The tools panel contains all the available tools to perform operations on the spectra.

As it can be seen in the tools panel, SpectPro provides several functionalities for spectra manipulation, including zoom, labeling, spectral shifting, baseline correction, spectral cutting, band fitting, normalization, and SNR (signal-to-noise ratio) calculation. After clicking on an operation, several configuration options are available.

In addition to those, the tools panel gives access to the spectral calculator. Through a specific interface, the spectral calculator offers a wide set of spectral operations which are useful for derivative analysis, intensity correction, or simply to perform linear combinations of spectra for differential calculations.

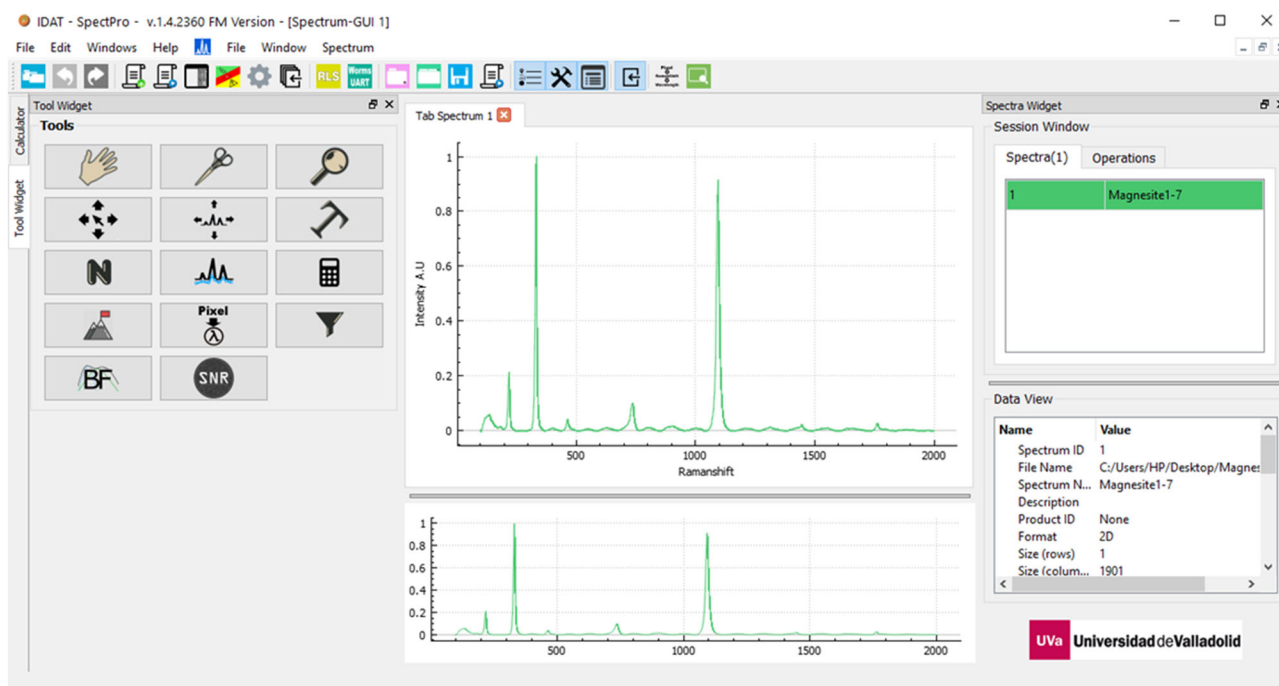


FIGURE 2 Main view of the SpectPro software (Analytical Database of Martian Minerals [ADaMM] version) with spectral tools [Colour figure can be viewed at wileyonlinelibrary.com]

As future improvements, an automated identification algorithm to classify Raman spectra will be also implemented. This algorithm is based on the comparison of peak positions and intensities, which has provided good results (a dedicated manuscript will be presented), even for the detection of multiple minerals present in simple mixtures.

## 4 | ADAMM MINERAL LIST

As the ADaMM database is meant to facilitate the interpretation of spectroscopic data returned by Mars 2020 and ExoMars rovers, mineral phases were selected by taking into account the main phases that are expected to be found at Jezero Crater and Oxia planum.

The detailed interpretation of Mars Express/OMEGA (Observatoire pour la Minéralogie, l'Eau, les Glaces, et l'Activité) and Mars Reconnaissance Orbiter/CRISM (Compact Reconnaissance Imaging Spectrometer for Mars) orbital data gathered from the two landing sites are provided elsewhere [25–30]. According to these works, both locations provide access to a wide variety of volcanic rocks formed during different geological periods. In general, it is well known that the mineralogical composition of Martian mafic regions is dominated by feldspar, pyroxene, and olivine minerals. However, from Noachian to Amazonian ages, magmatic rocks at the surface of Mars displayed a clear mineral transition towards higher concentrations of high-calcium pyroxene (HCP) and olivine phases [31, 32]. As such, unaltered volcanic rocks are an interesting scientific target for both Perseverance and Rosalind Franklin rovers, as their mineralogical and geochemical analyses would help detect mineralogical transitions between geological units, thus providing new analytical constraints to refine the mathematical models recently built to predict the thermochemical evolution of the mantle and the crust formation history of the planet [31].

Besides primary rocks, Jezero Crater and Oxia Planum also display several secondary minerals (e.g., carbonates [30]), most of which are widely acknowledged for being the result of water-rock interactions occurred during the Noachian period (phyllosilicates and hydrated silica) [33, 34]. As many alteration processes of volcanic rocks (e.g., hydrothermal [35]) are known to provide the key ingredients to sustain microbial proliferation and preservation of biomarkers, alteration deposits have been pointed out as priority scientific targets to meet the Mars 2020 and ExoMars goal to find traces of life on Mars.

Considering both primary and alteration mineral phases detected at Mars 2020 and ExoMars landing sites,

around 200 different mineral phases were chosen to be included to the ADaMM collection. In detail, the list of samples is mainly composed of natural specimens proceeding from the Geological and Mining Institute of Spain and the mineral collection of the University of Valladolid (Spain). Additional samples have been purchased from private collectors, and their authenticity has been corroborated by X-Ray diffractometry (XRD) analyses and petrological observations. As the ADaMM collection often includes more than one specimen for each mineral phase, the total number of samples is 320. However, the sample list will be periodically updated in order to reach a total of 250 mineral phases (and over 450 samples) by the end of the project (2022).

### 4.1 | Pyroxenes and pyroxenoids

Pyroxenes are inosilicate minerals with a crystalline structure consisting of single chains of silica tetrahedra. Their general formula is  $XY(\text{Si},\text{Al})_2\text{O}_6$ , where “X” represents Ca, Na, Fe, Mg, Li, or Mn ions, and “Y” represents Cr, Al, Fe, Mg, Mn, or Ti ions. Even though Na-rich (e.g., aegirine  $\text{NaFe}^{+3}\text{Si}_2\text{O}_6$  and jadeite  $\text{Na}[\text{Al},\text{Fe}^{3+}]\text{Si}_2\text{O}_6$ ) and Li-rich (spedumene  $\text{LiAl}[\text{SiO}_3]_2$ ) mineral species can be found, the majority of pyroxene minerals can be inscribed within a Ca-Fe-Mg ternary diagram, where wollastonite ( $\text{CaSiO}_3$ ), ferrosilite ( $\text{FeSiO}_3$ ), and enstatite ( $\text{MgSiO}_3$ ) are the endmember mineral phases. According to OMEGA orbital data, LCP (low-calcium) and HCP (high calcium) pyroxene minerals are widespread on the Martian surface [36]. The in situ analytical investigation carried out by exploration rovers, as well as the laboratory analysis of Martian meteorites, has provided more detailed information about pyroxene diversity on Mars, confirming the presence of the augite, pigeonite, enstatite, diopside, and bronzite mineral phases. The complete list of pyroxene minerals included in the ADaMM database is provided in Table 1, together with pyroxenoid phases (including wollastonite, rhodonite, and pectolite), which are single-chain silicates differing from pyroxenes by the twisted chain of silica tetrahedra that results in triclinic symmetry.

### 4.2 | Feldspars and feldspathoids

Feldspars are tectosilicate minerals whose elemental composition can be inscribed inside a Na-Ca-K ternary diagram, where orthoclase ( $\text{KAlSi}_3\text{O}_8$ ), albite ( $\text{NaAlSi}_3\text{O}_8$ ), and anorthite ( $\text{CaAl}_2\text{Si}_2\text{O}_8$ ) are the endmember mineral phases. Considering the miscibility gap between Ca and K, two solid solutions are possible:

TABLE 1 Provisional list of mineral samples included in the ADaMM database

<b>1 pyroxene-pyroxenoid</b>	Leucite	Omphacite	<b>8 Mn-Ti-Fe oxide and hydroxide</b>	Williamsite	<b>9e phyllosilicate sepiolite/paligorskite</b>	Phillipsite	Strontianite
<b>2 feldspar-feldspathoid</b>	Microcline	Riebeckite	<b>9b phyllosilicate mica</b>	Phyllosilicate mica	Phyllonite	Witherite	
Aegerine	Nepheline	Tremolite	Akaganeite	Williamsite	Paligorskite	Strontianite	
Augite	Nosean	<b>5 epidotes</b>	Anatase	Biotite	Sepiolite	Witherite	
Diopside	Oligoclase	Allanite	Bixbyite	Celadonite	9f phyllosilicate chlorite		
Enstatite	Orthoclase	Brookite	Brookite	Clintonite	Yugarwaralite	Aluminate	
Fassaite	Petalite	Clinozoisite	Goethite	Fuchsite	<b>11 carbonate</b>	Anglesite	
Hedenbergite	Sanidine	Epidote	Hematite	Glauconite	Clinocllore	Anhydrite	
Hypersthene	Sodalite	Hancockite	Ilmenite	Illite	Cookeite	Basanite	
Jadeite	Tugtupite	Piemontite	Jacobsite	Lepidolite	Pennantite	Botryogen	
Pectolite	<b>3 olivine</b>	<b>6 garnets</b>	Lepidocrocite	Margarite	Sudoite	Celestine	
Pyroxmangite			Maghemite	Muscovite	<b>10 zeolite</b>	Coquimbite	
Rhodonite	Fayalite	Almandine	Magnetite	Phlogopite	Azurite	Creedite	
Spodumene	Forsterite	Andradite	Pyrophanite	Zinnwaldite	Barytocalcite	Etringite	
Wollastonite	Knebelite	Grossular	Rutile	Xanthophyllite	Calcite	Felsobanyaite	
<b>2 feldspar-feldspathoid</b>	Tephroite	Pyrope	<b>9a phyllos. kaolinite/serpentine</b>	<b>9c phyllos. phyllophylite/Talc</b>	Clinoptilolite	Glauberite	
Albite	<b>4 amphibole</b>	Shorlomite	Antigorite	Phyllophylite	Epidesmine	Gypsum	
Amazonite	Actinolite	Spessartine	Bastite	Talc	Ferrierite	Halotrichite	
Analcime	Anthophyllite	Uvarovite	Chapmanite	<b>9d phyllosilicate smectite</b>	Gmelinite	Hanksite	
Anorthite	Arfvedsonite	<b>7 SiO2</b>	Chrysotile	Montmorillonite	Goosecreekite	Jarosite	
Anorthoclase	Bytownite	Aventurine	Deweyite	Nontronite	Harmotome	Kalinite	
Cancrinite	Cummingonite	Chalcedony	Dickite	Saponite	Heulandite	Melanterite	
Celsian	Ferroactinolite	Flint	Halloysite	Vermiculite	Laumontite	Natroalunite	
Hayne	Glaucophanite	Jasper	Kaolinite	Mordenite	Levyne	Natrojarosite	
Labradorite	Hornblende	Quartz	Lizardite	Natrolite	Maricopaite	Romerite	
Lazurite	Manganogrunerite	Picrolite			Rhodochrosite		

Abbreviation: ADaMM, Analytical Database of Martian Minerals.

minerals with a chemical composition between Ca- and Na-rich endmembers are known as plagioclases, while minerals between K and Na are named alkali-feldspar. Having a crystal structure similar to feldspars, feldspathoids (as sodalite, lazurite, and nosean) differ from them by their lower content of silica. As the capability of orbital instruments to detect feldspar and feldspathoids minerals on Mars is quite limited, most of the information related to these samples has been gathered from the rovers operating in situ and from the laboratory analysis of Martian meteorites. According to previous works, volcanic rocks on Mars present a wide mineral diversity from both alkali (e.g., sanidine) and plagioclase solid solutions series [37]. Considering the information available in the literature, 21 different feldspar and feldspathoid mineral species have been included into the ADaMM database (see Table 1).

### 4.3 | Olivines

Olivines are orthorhombic nesosilicates which general formula can be expressed as  $XYSiO_4$ , where X and Y correspond to ions such as Fe, Mg, and Mn. Both on Martian and Terrestrial rocks, the chemical composition of olivine can be described almost entirely by the binary ratio between Fe and Mg, thus placing most olivine minerals within the solid solution between endmembers forsterite (Fo,  $Mg_2SiO_4$ ) and fayalite (Fa,  $Fe_2SiO_4$ ). However, Martian olivine mostly differs from Terrestrial ones by their higher concentration of Fe, thus having a chemical composition close to fayalite. This information was extrapolated from OMEGA orbital data [38] and confirmed by laboratory analysis of Martian meteorites [39–41]. The ADaMM sample list provides access to several olivine samples within the forsterite-fayalite solid solutions (Table 1). In addition to those, it also contains tephroite ( $Mn_2SiO_4$ ) and knebelite ( $[Fe,Mn]_2SiO_4$ ) minerals, uncommon olivine phases rich in manganese.

### 4.4 | Amphiboles

Besides pyroxene, feldspar, and olivine phases, Martian igneous rocks also display minor abundances of amphiboles. For example, the Raman-based analysis of Zagami and Lewis Cliff 88516 Martian meteorites highlighted the presence of calcic amphibole minerals kaersutite and actinolite [42]. Phases belonging to this mineral group crystallize into both monoclinic and orthorhombic crystal systems. Chemically, amphiboles differ from pyroxenes as they contain essential hydroxyl (OH) or halogen (F, Cl). Mineralogically, their crystal structure differs for

being a double chain of silica tetrahedra. Although the minerals rich in Fe and Mg are the most abundant, these ions can be easily replaced by Li, Na, Mn, Ca, Zn, Co, Ti, and Al (among others), so that many different mineral phases can be found in nature. As shown in Table 1, the ADaMM database provides access to 12 different amphibole species.

### 4.5 | Epidotes

Within the group of sorosilicate, epidote describes a set of isomorphic series that crystallize in the monoclinic system. Rich in calcium, aluminum, and iron, the ideal formula of epidote is  $Ca_2FeAl_2(Si_2O_7)(SiO_4)O(OH)$ . However, ionic substitutions can occur, leading to the formation of further mineral phases. Thanks to the refined interpretation of NIR data collected from orbit, an Fe-rich epidote mineral phase was recently discovered on Mars and associated with hydrothermal, contact metasomatic, and low-grade metamorphic environments [43]. As presented below, five different mineral species from the epidote supergroup are included in the ADaMM database (Table 1).

### 4.6 | Garnets

Garnets are nesosilicates crystallizing in a cubic system and have the general formula  $X_3Y_2(SiO_4)_3$ , where X represents divalent cations as  $Ca^{2+}$ ,  $Mg^{2+}$ , and  $Fe^{2+}$  and  $Mn^{2+}$  and Y represents trivalent cations as  $Al^{3+}$ ,  $Fe^{3+}$ , and  $Cr^{3+}$ . Within this mineral group, the main mineral species are pyrope, almandine, spessartine, grossular uvarovite, and andradite. However, as partial elemental substitution can occur, different solid solution series are possible [44]. On Earth, garnets can be commonly found in metamorphic and igneous rocks, while their presence on Mars has been confirmed thanks to the laboratory analysis of SNC meteorites [45, 46]. As presented in Table 1, the above-mentioned endmember garnet species have been included into the ADaMM database.

### 4.7 | $SiO_2$

As observed from orbit, the great majority of the Martian crust is composed of basaltic rocks, whose elemental composition (low silica content) strongly limits the crystallization of Si-rich mineral phases (e.g., quartz). However, different varieties of  $SiO_2$  minerals were recently found on Mars. For example, a minor deposit of crystalline quartz was recently identified from orbit near

Antoniadi Crater, which was associated to the diagenetic product of amorphous silica [47]. More recently, the detection of tridymite (a low-pressure, high-temperature  $\text{SiO}_2$  mineral phase) by the XRD system onboard the Curiosity rover evidenced the past occurrence of Silicic volcanism episodes on Mars [48]. Focusing on Mars 2020 and ExoMars landing sites, the hydrated silica deposits (opaline,  $\text{SiO}_2 \cdot n\text{H}_2\text{O}$ ) detected at Jezero Crater [29] and Oxia Planum [33] are considered to be the alteration products of hydrothermal processes occurring in aqueous environments. As presented in Table 1, the ADaMM database includes an extended collection of crystalline (quartz), microcrystalline (chalcedony) and hydrated (opaline)  $\text{SiO}_2$  minerals.

#### 4.8 | Mn-Ti-Fe oxides and hydroxides

As iron is one of the predominant elements characterizing the geochemical composition of the Martian crust, several Fe-oxides and hydroxides can be found on Mars. In this context, critical analytical data were collected in situ by the Mössbauer spectrometers onboard the Spirit [49] and Opportunity [50] rovers. As proved in previous works, this analytical system enabled the detection of multiple Fe-bearing minerals, including oxide (e.g., hematite and magnetite) and hydroxide (goethite and ferrihydrite) phases [50]. In addition to these, the laboratory analysis of Martian meteorites enabled the identification of titanium-iron oxides such as ilmenite ( $\text{FeTiO}_3$ ) and titanomagnetite ( $(\text{Fe,Ti})_2\text{O}_4$ ) [51, 52]. Besides Ti- and Fe-rich minerals, high concentrations of manganese oxides have also been detected at Endeavor and Gale craters by the Opportunity and Curiosity rovers, respectively [53]. In light of the rich variety of oxide and hydroxide minerals found on Mars, the ADaMM database includes 14 different varieties of Fe-, Ti-, and Mn-based phases. However, this section is going to be further expanded by the end of the project.

#### 4.9 | Phyllosilicates

One of the main reasons driving the selection of Jezero Crater and Oxia Planum as landing sites of Mars 2020 and ExoMars missions is the abundant presence of phyllosilicate geological units resulting from the putative aqueous alteration of volcanic rocks. Phyllosilicates are known for being optimal scientific targets for astrobiological studies. Indeed, the crystalline structure of these hydrated minerals is formed by parallel sheets of silicate tetrahedra that can accumulate organic

molecules between layers and preserve them from external alteration processes [54]. Therefore, the ADaMM list includes around 100 samples representing over 50 different phyllosilicate minerals phases. As presented in Table 1, the database includes specimens from the following subgroups: kaolinite/serpentine (11 mineral phases), sepiolite/paligorskite (2), smectite (4), mica (12), chlorite (5), and pyrophyllite/talc (2).

#### 4.10 | Zeolites

Zeolites are aluminosilicate minerals composed of tetrahedra formed by one cation (either Al or Si) connected to four oxygens. As presented elsewhere, zeolite minerals as clinoptilolite and chabazite were found to be one of the mineral components of Martian dust [55, 56] and their presence has been interpreted as the result of water-related weathering of primary Martian minerals [57]. Similarly to phyllosilicates, zeolites have great scientific relevance for astrobiological studies, as their porous structure is capable of absorbing water molecules. For this reason, a wide variety of zeolite minerals from the natrolite, analcime, gismondine, hermatome, helandite, and natronite families have been included in the ADaMM database.

#### 4.11 | Carbonates

Seen from orbit, the surface of Mars additionally presents minor carbonate rocks which mineralogical composition can be inscribed within the Ca-Fe-Mg ternary system, where calcite ( $\text{CaCO}_3$ ), siderite ( $\text{FeCO}_3$ ), and magnetite ( $\text{MgCO}_3$ ) represent the endmember mineral phases. For instance, Fe-Mg carbonates were detected by the Spirit rover in the Columbia Hills of Gusev crater [58]. Focusing on the landing sites, the elevation of the carbonates detected at the margins of Jezero crater suggests that their deposition occurred during the closed-basin phase of the lake sequence [30]. Although orbital data from Oxia Planum did not reveal carbonate deposits, carbonate precipitates are expected to be found at a microscale by the Rosalind Franklin rover as they are often found associated to phyllosilicates (which cover 70% of the landing site) in aqueous environments [59]. Knowing that carbonate precipitation is widely recognized as an excellent mechanism for bio-signature preservation [60], carbonate minerals on Mars are considered a valuable analytical target for both Mars 2020 and ExoMars rovers. As presented in Table 1, the database includes 21 different carbonate minerals, both anhydrous and hydrated.



## 4.12 | Sulfates

The sulfate ion ( $\text{SO}_4^{2-}$ ) has a tetrahedral structure consisting of a central sulfur atom surrounded by four oxygens. Depending on the cation(s) bounded to the sulfate, different minerals are formed. Focusing on Mars, orbital observations by OMEGA and CRISM provided clear evidences of Fe-, Ca-, and Fe-rich sulfate deposits [61]. Opportunity and Curiosity rovers further confirmed the detection of partially hydrated sulfate minerals at Meridiani Planum [62] and Gale crater [63, 64], respectively. More recently, the refined interpretation of CRISM hyperspectral data enabled the detection at the Mars 2020 landing site of jarosite, an Fe-rich sulfate generally precipitated from hydrothermal acidic ( $\text{pH} < 4$ ) solutions rich in heavy metals [65]. Considering the multiple sulfate minerals so far detected on Mars, the ADaMM database includes 21 anhydrous and hydrated sulfates.

## 5 | RAMAN INSTRUMENTS

The whole set of mineral phases described in Section 3 was analyzed by means of both diffractometric (XRD) and spectroscopic (FTIR, LIBS, Raman) techniques. However, being this work mainly focused on Raman data, the present section only describes the Raman analytical systems employed in this work.

### 5.1 | Conventional Raman systems

At first, all mineral patterns were analyzed by a combination of conventional laboratory systems that mainly differ on the excitation wavelength.

Concretely, the MicroRaman system is composed of a Research Electro-Optics LSRP-3501 excitation laser (Helium–Neon) emitting at 633 nm, a KOSI HoloSpec1.8i spectrometer, and an Andor DV420A-OE-130 CCD detector. The Nikon Eclipse E600 microscope coupled to the system is equipped with interchangeable long WD objectives of 5 $\times$ , 10 $\times$ , 20 $\times$ , 50 $\times$ , and 100 $\times$  (down to a spot size of 10  $\mu\text{m}$ ). The system works in a double track mode covering a spectral range between 130 and 3780  $\text{cm}^{-1}$ , with an average spectral resolution of 5  $\text{cm}^{-1}$ .

Further Raman analyses were performed with the Induram system (Horiba-JY). The instrument is composed of a green excitation source (Laser Elforlight G4-30 PSU, emitting at 532 nm), while the spectrometer and the CCD detector are from a Horiba-JY Induram industrial Raman system. As in the case of the MicroRaman, the Raman probe is coupled to a microscope (Zeiss Axiotech 30), which focuses on the sample through a

long WD objective of 50 $\times$  (spot size of 50  $\mu\text{m}$ ). In this case, Raman spectra were collected from 100 to 4000  $\text{cm}^{-1}$  with a mean spectral resolution of 4  $\text{cm}^{-1}$ .

Selected mineral samples were additionally characterized with the IFS 66 FT-Raman system (Bruker) coupled to an FRA 106 Raman module attachment. In this case, the excitation source is a Nd<sup>3++</sup>YAG laser emitting at 1064 nm while the sample ‘footprint’ at the focus of the laser beam is about 100 mm in diameter. Raman spectra were collected from 100 to 4000  $\text{cm}^{-1}$  with a mean spectral resolution of 8  $\text{cm}^{-1}$ .

### 5.2 | Raman prototypes emulating planetary exploration systems

Being directly involved in the development of the SuperCam and RLS spectrometers onboard the Perseverance and Rosalind Franklin rovers, the ERICA group (Espectroscopía Raman e Infrarroja aplicado a Cosmogeología y Astrobiología) assembled a set of representative Raman prototypes that collect spectra qualitatively comparable to those that the flight models will gather on Mars, while avoiding the technical-operational limitations imposed by the management of instrumentation developed for space exploration.

The RLS ExoMars Simulator [66] is composed of a continuous laser source emitting at 532 nm, a high-resolution TE Cooled CCD Array spectrometer, and an optical head with a long WD objective of 50 $\times$ . The range of analysis (70–4200  $\text{cm}^{-1}$ ), working distance ( $\approx 15$  mm), laser power output (20 mW), spot of analysis ( $\approx 50$   $\mu\text{m}$ ), spectral resolution (6–10  $\text{cm}^{-1}$ ), and SNR of this instrument closely resemble those of the RLS instrument. Software-wise, the RLS ExoMars Simulator integrates the same algorithms implemented by the RLS to autonomously operate on Mars, such as dark subtraction, fluorescence quenching, and acquisition parameters optimization [67]. This instrument represents the key analytical tool for the RLS science team to investigate the potential scientific capability of the flight model soon operating on Mars. As such, recent research confirmed the capability of the RLS ExoMars Simulator to (1) detect biomarkers in extreme environments [68], (2) identify shock-related metamorphism of impacted minerals [69], (3) extrapolate the elemental composition of mineral phases within solid solution series [70], and (4) extrapolate semiquantitative values through the chemometric analysis of ExoMars-like Raman datasets (39 spectra per sample) [71, 72].

To reliably simulate the scientific outcome of SuperCam, a remote Raman-LIBS system was used. This instrument uses a Nd:YAG laser, frequency-doubled to

provide a 532-nm excitation source. The laser is delivered to the sample collimated, providing a constant irradiance with distance. The Raman emission is collected at 5-m distance by an SLR Lens (300 mm focal,  $f$ : 4–5 mm) and delivered to a two-track spectrometer covering a range between 100 and 4000  $\text{cm}^{-1}$  with a mean spectral resolution of 10  $\text{cm}^{-1}$ . The instrument has been optimized to obtain remote Raman spectra (spot size around 500  $\mu\text{m}$ ) with an SNR comparable to the SuperCam instrument. Its first use as terrestrial simulator of the Mars 2020 remote spectrometer has been recently presented elsewhere [73, 74].

The acquisition parameters set for Raman analyses vary according to the employed spectrometer and the sample characteristics. Regarding environmental conditions, most Raman analyses were performed under terrestrial temperature and pressure conditions. However, the RLS ExoMars Simulator was also used to perform additional investigations under Martian environmental conditions. For this purpose, the Raman spectrometer was coupled to a thermal cell (Linkam), composed of the following components: a FDSC196 cryostage (enabling temperature monitoring and control within a working range from +125 to  $-196^\circ\text{C}$ ), a T96 temperature control (used to program temperature ramps), a LNP96 liquid nitrogen pump and Dewar, a Pirani vacuum gauge (enabling pressure control within a working range from atmospheric to  $10^{-4}$  mBar), a Leybold D2.5E rotary vane vacuum pump, and a dedicated workstation.

Raman spectra were visualized by using the IDAT/SpectPro software described in section 3. Knowing that quantum efficiency of CCD detectors varies with wavelength, all Raman spectra were intensity-corrected by following the method by Sanz-Arranz et al. [75] As the minerals presented in the following section did not display any fluorescence issue, no data treatment was applied. However, it is important to underline that the research group is using further ADaMM samples to discriminate fluorescence in Mars-relevant minerals and those results will be published elsewhere.

## 6 | A CASE OF STUDY: CA-FE-MG CARBONATES

Raman spectra gathered from carbonate minerals present several vibrational peaks that can be classified into two main types. On the one hand, the excitation of the  $(\text{CO}_3)^{2-}$  group gives rise to four internal vibrational modes: being the main peak in the Raman spectra (between 1080 and 1120  $\text{cm}^{-1}$ ), the  $\nu_1$  mode is produced by the nondegenerate symmetric stretch of the carbonate ion. The  $\nu_2$  mode (near 800  $\text{cm}^{-1}$ , mostly IR active) is

derived from the symmetric bending mode, while asymmetric stretching ( $\nu_3$ ) and bending ( $\nu_4$ ) modes produce weak Raman signals around 1450 and 700  $\text{cm}^{-1}$ , respectively [76]. In addition to these, a weak signal can also be observed around 1750  $\text{cm}^{-1}$ , which may be regarded as the combination bands of  $\nu_1 + \nu_4$  modes [77]. On the other hand, M-O vibration modes are due to the interactions between the cations of the crystal lattice and the oxygens from the  $(\text{CO}_3)^{2-}$  group. These vibrational modes favor the emission of several peaks of medium intensity that generally appear at wavelengths below 350  $\text{cm}^{-1}$ . Here, peaks appearing at lower wavenumbers (between 150 and 220  $\text{cm}^{-1}$ ) are assigned to translational modes ( $T$ ), while librational modes ( $L$ ) appear in a range between 200 and 340  $\text{cm}^{-1}$  [78].

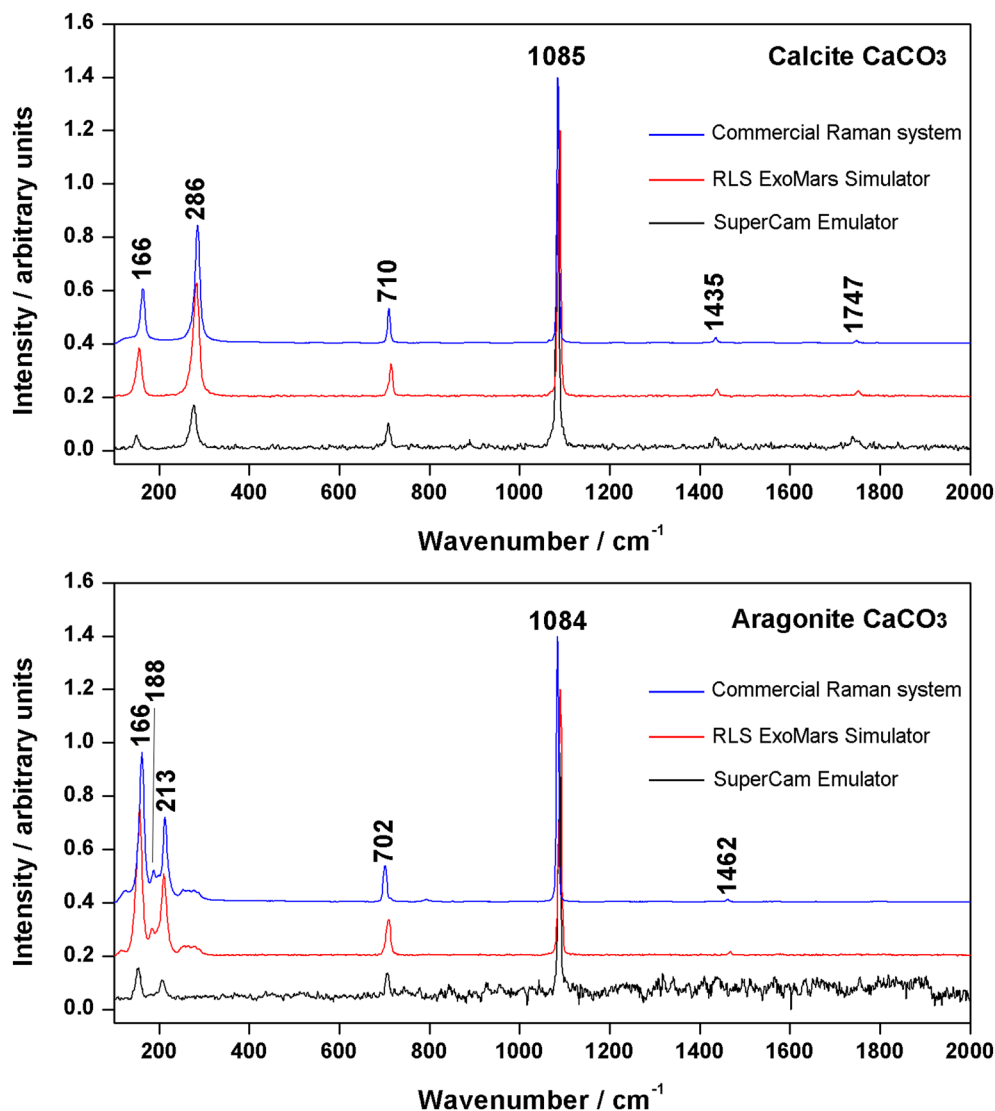
As the vibrational modes of carbonate minerals are affected in different degrees as a consequence of cation substitution [76, 79], the Raman spectra of Ca-Fe-Mg carbonates are here analyzed and compared, these being the minerals phases that are expected to be found at the landing sites of Mars 2020 and ExoMars missions. In detail, knowing the different analytical performances of Raman systems developed for planetary missions over state-of-the-art laboratory systems, the Raman spectra gathered from the use of the RLS ExoMars Simulator and a Remote Raman prototype emulating the Mars 2020/SuperCam system were compared with those provided by the InduRam commercial spectrometer.

### 6.1 | Calcite–aragonite

Calcium carbonate ( $\text{CaCO}_3$ ) can crystallize under different structures or polymorphs: calcite (trigonal crystal system), aragonite (orthorhombic) and vaterite (hexagonal). Being the most commonly occurring  $\text{CaCO}_3$  minerals in nature, the Raman spectra of calcite and aragonite are provided in Figure 3. The Raman spectra comparison shows that, when analyzing pure mineral phases, all the main vibrational modes of both calcite and aragonite can be effectively detected by both the RLS ExoMars Simulator and the SuperCam laboratory prototype. Starting from calcite, the three instruments clearly detected the internal vibrational mode at 710 ( $\nu_4$ ), 1085 ( $\nu_1$ ), 1435 ( $\nu_3$ ), and 1747  $\text{cm}^{-1}$  ( $\nu_1 + \nu_4$ ). Concerning external modes,  $T$  and  $L$  Raman peaks were found around 166 and 286  $\text{cm}^{-1}$ , respectively.

Concerning the aragonite standard, both the commercial Raman system and the RLS ExoMars Simulator detected  $T$  (double peak at 166 and 188  $\text{cm}^{-1}$ ),  $L$  (213  $\text{cm}^{-1}$ ),  $\nu_1$  (1,084  $\text{cm}^{-1}$ ),  $\nu_3$  (1,462  $\text{cm}^{-1}$ ), and  $\nu_4$  (702  $\text{cm}^{-1}$ ) vibrational modes. Compared with these, the lower SNR of the Raman spectrum collected

**FIGURE 3** Raman spectra of calcite and aragonite [Colour figure can be viewed at [wileyonlinelibrary.com](http://wileyonlinelibrary.com)]



by the Remote Raman system from a SuperCam-representative working distance of 5 m, impeded the detection of the  $\nu_2$  mode. As the key spectral feature differentiating aragonite from calcite is produced by the librational mode (peak shift of  $73 \text{ cm}^{-1}$ ), it can be inferred that the proper discrimination between  $\text{CaCO}_3$  polymorphs on Mars will rely on the detection of secondary Raman peaks [80, 81].

## 6.2 | Dolomite–ankerite

Along the calcium-manganese axis of the Ca-Fe-Mg ternary system, dolomite  $\text{CaMg}(\text{CO}_3)_2$  is a double carbonate crystallizing in trigonal system. As displayed in Figure 4, the main Raman peaks of this mineral phase are found at 185, 304, 343, 723, 1094, 1442,  $1755 \text{ cm}^{-1}$ . Compared with  $\text{CaCO}_3$  polymorphs, dolomite can be clearly distinguished by the marked shift of the main vibrational

peak ( $\nu_1$ ) towards higher wavenumbers ( $+ 10 \text{ cm}^{-1}$ ). Similarly, the degree of peak shifting observed on the two main external vibrational modes ( $185$  and  $304 \text{ cm}^{-1}$ ) should be easily detected by RLS and SuperCam when analyzing pure minerals.

As presented elsewhere, Mg can be partially substituted by Fe, originating a solid solution between the endmembers dolomite and ankerite (ideally  $\text{CaFe}(\text{CO}_3)_2$ ). As pure ankerite samples cannot be found in nature [82], the ankerite specimens included to the ADaMM database refer to carbonate minerals with a high degree of Mg-Fe substitution. Compared with dolomite, Figure 4 shows the main Raman peak of ankerite slightly shifts towards higher wavenumbers (from  $1094$  to  $1097 \text{ cm}^{-1}$ ), while the external modes shift in the opposite direction (to  $181$  and  $294 \text{ cm}^{-1}$ ).

As reported in previous works, the linear correlation between peak shifting and the iron substitution can be used to estimate the elemental composition of mineral

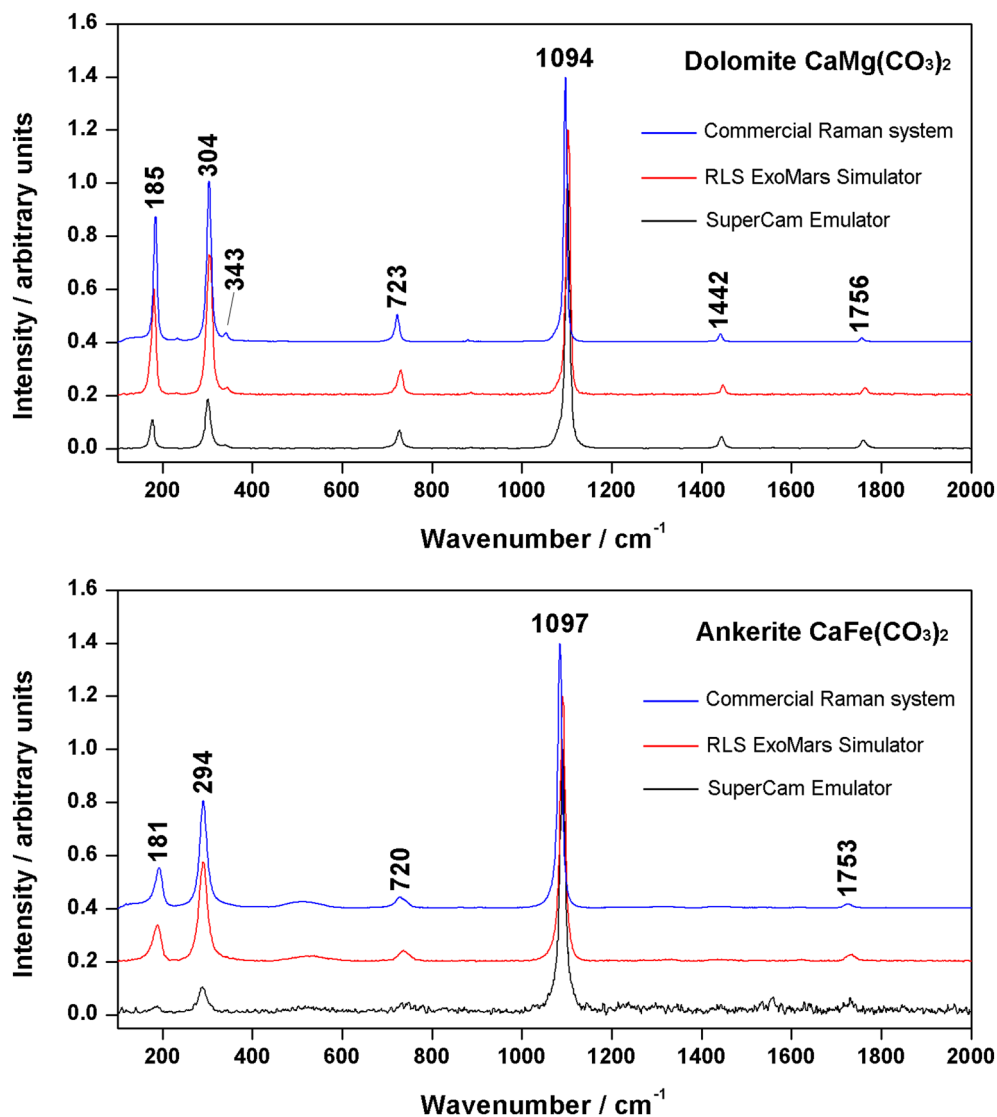


FIGURE 4 Raman spectra of dolomite and ankerite [Colour figure can be viewed at [wileyonlinelibrary.com](http://wileyonlinelibrary.com)]

phases from the dolomite-ankerite solid solution [79]. Focusing on Mars 2020 and ExoMars missions, tailored RLS and SuperCam models can be developed taking into account the analytical performance and the operational constraints of the two analytical instruments. For this purpose, it is important to determine the spectroscopic features that are more likely to be detected on Mars. In this sense, Figure 4 shows that the RLS Simulator effectively detected all major peaks, while the analysis of iron-rich carbonate samples performed by the SuperCam emulator lacked the detection of minor vibrational modes. The low quality of the SuperCam-like spectrum gathered from the ankerite standard is strongly related to the mineral color. Indeed, when analyzing dark targets (as is the case of ankerite), most of the incident (laser excitation source) and scattered light (including Raman signal) is absorbed by the sample and converted into thermal energy. Therefore, with similar measurement conditions, light-colored minerals generally have better

scattering efficiency than dark ones [15]. When using conventional Raman systems, this limitation can be partially compensated by setting longer accumulation times. However, this solution is less effective for remote systems, where sample excitation is triggered by short laser pulses (on the order of ns). In addition to that, the working distance for conventional Raman systems is about a few mm, so that the efficiency of Raman signal detection is much higher than on remote systems, where there are several meters distance between the target and the lenses collecting the Raman signal.

### 6.3 | Huntite

Besides dolomite, an additional double carbonate crystallizes along the Ca-Mg axis of the ternary carbonate system. Known as huntite ( $\text{CaMg}_3(\text{CO}_3)_4$ ), its characteristic Raman spectrum can be clearly distinguished from other

Mg-Fe-Ca carbonates by the position of its  $\nu_1$  peak ( $1120\text{ cm}^{-1}$ ). As displayed in Figure 5, other differences are found in the area of the external vibrational modes,

where up to five Raman peaks can be detected ( $126, 163, 256, 276,$  and  $318\text{ cm}^{-1}$ ). Furthermore, this mineral also displays a clear additional signal at  $876\text{ cm}^{-1}$ , which can

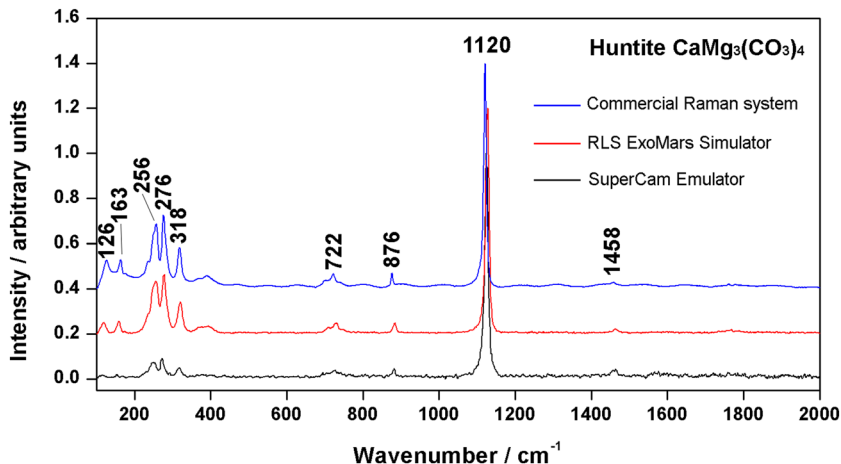


**FIGURE 5** Raman spectra of huntite [Colour figure can be viewed at [wileyonlinelibrary.com](http://wileyonlinelibrary.com)]

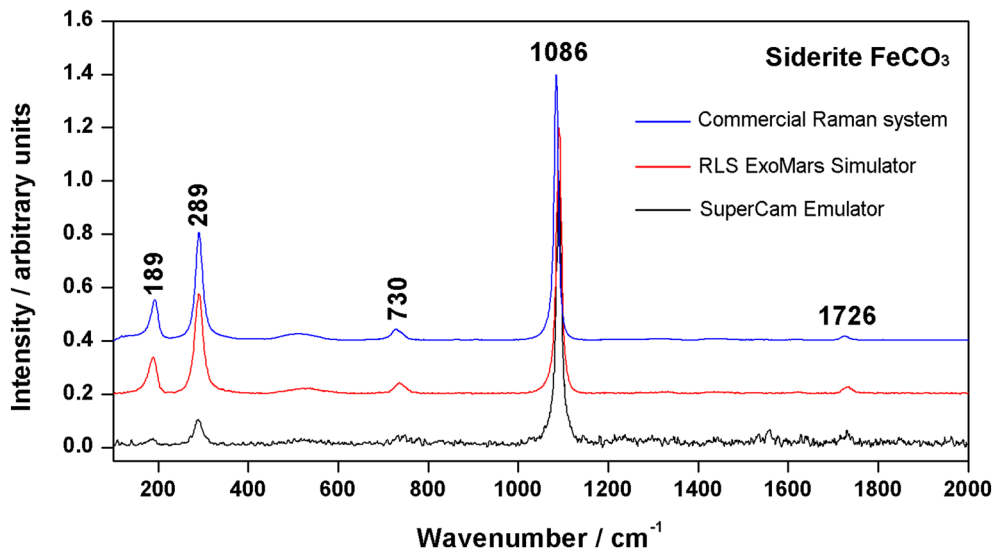
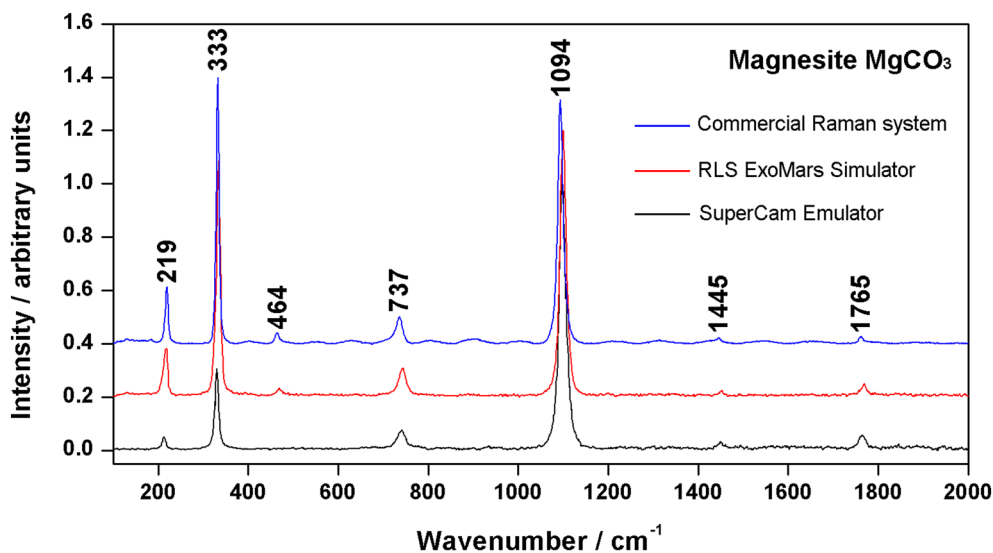


**FIGURE 6** Raman spectra of magnesite and siderite [Colour figure can be viewed at [wileyonlinelibrary.com](http://wileyonlinelibrary.com)]

be assigned to the  $\nu_2$  symmetric bending mode of the  $\text{CO}_3^-$  group [76, 83]. High-quality spectra were collected by the three spectrometers. However, the lower sensitivity of the Raman prototype at lower wavelengths impeded the clear detection of translational modes ( $126$  and  $163\text{ cm}^{-1}$ , which position has a strong dependence on the cation mass [84]).

## 6.4 | Magnesite-siderite

The magnesium and iron endmembers of the Ca-Fe-Mg carbonate system are magnesite ( $\text{MgCO}_3$ ) and siderite ( $\text{FeCO}_3$ ), respectively. On the one hand, the main  $T$  and  $L$  external modes of magnesite are clearly detected at  $219$  and  $333\text{ cm}^{-1}$ , while the internal modes can be found at  $737$  ( $\nu_4$ ),  $1094$  ( $\nu_1$ ),  $1445$  ( $\nu_3$ ), and  $1765\text{ cm}^{-1}$  ( $\nu_1 + \nu_4$ ). Even though the position of  $\nu_1$  peak is the same as for dolomite ( $1094\text{ cm}^{-1}$ ), magnesite can be clearly distinguished from all other carbonates within the ternary system by the higher wavenumber position of the librational peak, which is detected at  $333\text{ cm}^{-1}$  (Figure 6).

The main peak of siderite is found at  $1086\text{ cm}^{-1}$ , this position being very similar to the characteristic  $\nu_1$  modes of calcium carbonate polymorphs ( $1084$  and  $1085\text{ cm}^{-1}$  for calcite and aragonite, respectively). Regarding external vibrational modes, the position of the main librational peak is also similar to the calcite one ( $286$  vs  $289\text{ cm}^{-1}$ ) so that the third main peak ( $T$  mode at  $189\text{ cm}^{-1}$ ) is of key importance for the proper Raman discrimination of this mineral phase. As displayed in Figure 6, this peak was barely detected by the remote Raman prototype due to the dark color of the mineral (as was the case for ankerite) as well as the low sensitivity of the employed spectrometer at low wavelengths. However, in light of the Mars 2020 mission, it must be underlined that the lower quality of Raman spectra remotely collected by SuperCam from dark targets can be effectively compensated by the complementary data provided by LIBS and luminescence spectra this instrument is capable of collecting from the same spot of analysis. On one side, LIBS data provide information on the elemental composition of the analyzed target, while the characterization of mineral luminescence can disclose the presence of transition metals and certain rare-earth elements (REEs) [85, 86].

Similar to the case of the dolomite-ankerite solid solution, the partial substitution of Mg by Fe on magnesite gives rise to a solid solution series between magnesite and ankerite endmembers. By evaluating the correlation between peak shifting and iron content, previous works proved that the position of secondary peaks from external vibrational modes around  $195$  ( $T$ ) and  $300\text{ cm}^{-1}$  ( $L$ ) is

more effective than  $\nu$  signals in the proper estimation of the Mg/Fe ratio of mineral phases within this solid solution [87].

In light of the forthcoming deployment of Rosalind Franklin, as well as the ongoing operation of the Perseverance rover on Mars, the detection of secondary Raman signals emitted by external vibrational modes will play a key role in the in-depth analysis of carbonate mineral phases on Mars.

## 7 | CONCLUSIONS

This work has provided a general overview of the ADaMM database, which is planned to be released to the public in 2022. The structure of the online platform that is being developed to provide future users with free access to the database has been described in Section 2. Section 3 presented the main functionalities of SpectPro, a tailored spectral software tool coupled to the ADaMM platform and developed in the framework of the ExoMars mission to visualize and manipulate the analytical data returned from the RLS instrument. The detailed list of the mineral phases included in the ADaMM database has been provided in Section 4, while Section 5 presented the Raman instruments employed for their characterization. As the main characteristic of the ADaMM project is to provide analytical data gathered from both commercial systems and laboratory prototypes emulating the analytical performances of the spectroscopic tools onboard the Perseverance and Rosalind Franklin rovers, the usefulness of accessing data qualitatively comparable to those gathered by RLS and SuperCam has been demonstrated with representative examples.

In detail, Section 6 presented a multi-instrumental Raman comparison of carbonates within the Ca-Fe-Mg system. The provided results suggested that the Raman discrimination of carbonate mineral phases on Mars is possible as long as secondary peaks emitted by the external vibrational modes  $T$  and  $L$  are detected. In this sense, the comparison between the RLS ExoMars Simulator and the pulsed Raman prototype emulating SuperCam showed that the efficiency of the Raman signal detection strongly decreased when dark mineral targets were remotely investigated. Even though laboratory prototypes have been optimized to provide results qualitatively similar to Mars 2020 and ExoMars spectrometers, the collected data are not perfectly equal to those gathered by flight instruments. For this reason, the ADaMM database will be further optimized in the forthcoming years, by including the Raman analysis of selected ADaMM minerals by the RLS spare model. Once released to the public, the ADaMM database will provide unique tailored

tools that will help the scientific community to optimize the analytical exploitation of Martian spectroscopic data.

## ACKNOWLEDGEMENTS

This work is funded by the H2020 European Research Council (grant 687302) and the Ministry of Economy and Competitiveness (MINECO, grant PID2019-107442RB-C31).

## DATA AVAILABILITY STATEMENT

The data that support the findings of this study are available from the corresponding author upon reasonable request.

## ORCID

Marco Veneranda  <https://orcid.org/0000-0002-7185-2791>

Emmanuel Lalla  <https://orcid.org/0000-0002-0005-1006>

Andoni Moral  <https://orcid.org/0000-0002-6190-8560>

Guillermo Lopez-Reyes  <https://orcid.org/0000-0003-1005-1760>

## REFERENCES

- [1] K. A. Farley, K. H. Williford, K. M. Stack, R. Bhartia, A. Chen, M. de la Torre, K. Hand, Y. Goreva, C. D. K. Herd, R. Hueso, Y. Liu, J. N. Maki, G. Martinez, R. C. Moeller, A. Nelessen, C. E. Newman, D. Nunes, A. Ponce, N. Spanovich, P. A. Willis, L. W. Beegle, J. F. Bell, A. J. Brown, S. E. Hamran, J. A. Hurowitz, S. Maurice, D. A. Paige, J. A. Rodriguez-Manfredi, M. Schulte, R. C. Wiens, *Space Sci. Rev.* **2020**, *216*, 142.
- [2] K. H. Williford, K. A. Farley, K. M. Stack, A. C. Allwood, D. Beaty, L. W. Beegle, R. Bhartia, A. J. Brown, M. de la Torre Juarez, S.-E. Hamran, M. H. Hecht, J. A. Hurowitz, J. A. Rodriguez-Manfredi, S. Maurice, S. Milkovich, R. C. Wiens, *The NASA Mars 2020 Rover Mission and the Search for Extraterrestrial Life*, Elsevier Inc., Amsterdam, 1 st **2018**.
- [3] R. C. Wiens, S. Maurice, F. R. Perez, *Spectrosc. (Santa Monica)* **2017**, *32*, 50.
- [4] J. A. Manrique, G. Lopez-Reyes, A. Cousin, F. Rull, S. Maurice, R. C. Wiens, M. B. Madsen, J. M. Madariaga, O. Gasnault, J. Aramendia, G. Arana, P. Beck, S. Bernard, P. Bernardi, M. H. Bernt, A. Berrocal, O. Beyssac, P. Caïs, C. Castro, K. Castro, S. M. Clegg, E. Cloutis, G. Dromart, C. Drouet, B. Dubois, D. Escribano, C. Fabre, A. Fernandez, O. Forni, V. Garcia-Baonza, I. Gontijo, J. Johnson, J. Laserna, J. Lasue, S. Madsen, E. Mateo-Marti, J. Medina, P. Y. Meslin, G. Montagnac, A. Moral, J. Moros, A. M. Ollila, C. Ortega, O. Prieto-Ballesteros, J. M. Reess, S. Robinson, J. Rodriguez, J. Saiz, J. A. Sanz-Arranz, I. Sard, V. Sautter, P. Sobron, M. Toplis, M. Veneranda, *Space Sci. Rev.* **2020**, *216*, 1.
- [5] A. C. Allwood, L. A. Wade, M. C. Foote, W. T. Elam, J. A. Hurowitz, S. Battel, D. E. Dawson, R. W. Denise, E. M. Ek, M. S. Gilbert, M. E. King, C. C. Liebe, T. Parker, D. A. K. Pedersen, D. P. Randall, R. F. Sharrow, M. E. Sondheim, G. Allen, K. Arnett, M. H. Au, C. Basset, M. Benn, J. C. Bousman, D. Braun, R. J. Calvet, B. Clark, L. Cinquini, S. Conaby, H. A. Conley, S. Davidoff, J. Delaney, T. Denver, E. Diaz, G. B. Doran, J. Ervin, M. Evans, D. O. Flannery, N. Gao, J. Gross, J. Grotzinger, B. Hannah, J. T. Harris, C. M. Harris, Y. He, C. M. Heirwegh, C. Hernandez, E. Hertzberg, R. P. Hodyss, J. R. Holden, C. Hummel, M. A. Jadusingsh, J. L. Jørgensen, J. H. Kawamura, A. Kitiyakara, K. Kozaczek, J. L. Lambert, P. R. Lawson, Y. Liu, T. S. Luchik, K. M. Macneal, S. N. Madsen, S. M. McLennan, P. McNally, P. L. Meras, R. E. Muller, J. Napoli, B. J. Naylor, P. Nemere, I. Ponomarev, R. M. Perez, N. Pootrakul, R. A. Romero, R. Rosas, J. Sachs, R. T. Schaefer, M. E. Schein, T. P. Setterfield, V. Singh, E. Song, M. M. Soria, P. C. Stek, N. R. Tallarida, D. R. Thompson, M. M. Tice, L. Timmermann, V. Torossian, A. Treiman, S. Tsai, K. Uckert, J. Villalvazo, M. Wang, D. W. Wilson, S. C. Worel, P. Zamani, M. Zappe, F. Zhong, R. Zimmerman, *Space Sci. Rev.* **2020**, *216*, 134.
- [6] L. Beegle, R. Bhartia, M. White, L. Deflores, W. Abbey, Y. H. Wu, B. Cameron, J. Moore, M. Fries, A. Burton, K. S. Edgett, M. A. Ravine, W. Hug, R. Reid, T. Nelson, S. Clegg, R. Wiens, S. Asher, P. Sobron, *IEEE Aerospace Conference Proceedings* **2015**, p. 1.
- [7] J. L. Vago, F. Westall, A. J. Coates, R. Jaumann, O. Korablev, V. Ciarletti, I. Mitrofanov, J. L. Josset, M. C. De Sanctis, J. P. Bibring, F. Rull, F. Goesmann, H. Steininger, W. Goetz, W. Brinckerhoff, C. Szopa, F. Raulin, H. G. M. Edwards, L. G. Whyte, A. G. Fairén, J. Bridges, E. Hauber, G. G. Ori, S. Werner, D. Loizeau, R. O. Kuzmin, R. M. E. Williams, J. Flahaut, F. Forget, D. Rodionov, H. Svedhem, E. Sefton-Nash, G. Kmínek, L. Lorenzoni, L. Joudrier, V. Mikhailov, A. Zashchirinskiy, S. Alexashkin, F. Calantropio, A. Merlo, P. Poulakis, O. Witasse, O. Bayle, S. Bayón, U. Meierhenrich, J. Carter, J. M. García-Ruiz, P. Baglioni, A. Haldemann, A. J. Ball, A. Debus, R. Lindner, F. Haessig, D. Monteiro, R. Trautner, C. Volland, P. Rebeyre, D. Gouly, F. Didot, S. Durrant, E. Zekri, D. Koschny, A. Toni, G. Visentin, M. Zwick, M. Van Winnendael, M. Azkarate, C. Carreau, *Astrobiology* **2017**, *17*, 471.
- [8] F. Goesmann, W. B. Brinckerhoff, F. Raulin, W. Goetz, R. M. Danell, S. A. Getty, S. Siljeström, H. Mißbach, H. Steininger, R. D. Arevalo, A. Buch, C. Freissinet, A. Grubisic, U. J. Meierhenrich, V. T. Pinnick, F. Stalport, C. Szopa, J. L. Vago, R. Lindner, M. D. Schulte, J. R. Brucato, D. P. Glavin, N. Grand, X. Li, F. H. W. Van Amerom, *Astrobiology* **2017**, *17*, 655.
- [9] J. P. Bibring, V. Hamm, C. Pilorget, J. L. Vago, M. Team, *Astrobiology* **2017**, *17*, 621.
- [10] F. Rull, S. Maurice, I. Hutchinson, A. Moral, C. Perez, C. Diaz, M. Colombo, T. Belenguer, G. Lopez-Reyes, A. Sansano, O. Forni, Y. Parot, N. Striebig, S. Woodward, C. Howe, N. Tarcea, P. Rodriguez, L. Seoane, A. Santiago, J. A. Rodriguez-Prieto, J. Medina, P. Gallego, R. Canchal, P. Santamaría, G. Ramos, J. L. Vago, *Astrobiology* **2017**, *17*, 627.
- [11] T. Usui, K. i. Bajo, W. Fujiya, Y. Furukawa, M. Koike, Y. N. Miura, H. Sugahara, S. Tachibana, Y. Takano, K. Kuramoto, *Space Sci. Rev.* **2020**, *216*, 49.
- [12] S. Schröder, T. Belenguer, U. Böttger, M. Buder, Y. Cho, E. Dietz, M. Gensch, T. Hagelschuer, F. Hanke, H.-W. Hübers, S. Kameda, E. Kopp, S. Kubitzka, A. Moral, C. Paproth, M. Pertenais, G. Peter, K. Rammelkamp, P. Rodriguez, F. Rull,

- C. Ryan, T. Säuberlich, F. Schrandt, S. Ulamec, T. Usui, R. Vance, *51st Lunar and Planetary Science Conference*, The Woodlands, Texas **2020**, p. 2019.
- [13] C. B. Phillips, K. P. Hand, M. L. Cable, A. E. Hofmann, K. L. Craft, *50th Lunar and Planetary Science Conference*, The Woodlands, Texas **2019**, p. 2685.
- [14] S. K. Sharma, J. N. Porter, A. K. Misra, T. E. Acosta-Maeda, S. M. Angel, C. P. McKay, *J. Raman Spectrosc* **2020**, *51*, 1782.
- [15] S. M. Angel, N. R. Gomer, S. K. Sharma, C. McKay, N. Ames, *Appl. Spectrosc.* **2012**, *66*, 137.
- [16] C. Lantz, F. Poulet, D. Loizeau, L. Riu, C. Pilorget, J. Carter, H. Dypvik, F. Rull, S. C. Werner, *Planet. Space Sci.* **2020**, *189*, 104989.
- [17] D. Loizeau, G. Lequertier, F. Poulet, V. Hamm, C. Pilorget, L. Meslier-Lourit, C. Lantz, S. C. Werner, F. Rull, J. P. Bibring, *Planet. Space Sci.* **2020**, *193*, 105087.
- [18] M. Veneranda, J. Sáiz, A. Sanz-Arranz, J. A. Manrique, G. Lopez-Reyes, J. Medina, H. Dypvik, S. C. Werner, F. Rull, *J. Raman Spectrosc.* **2019**, *51*, 1731.
- [19] B. Lafuente, R. T. Downs, H. Yang, N. Stone, in *Highlights in Mineralogical Crystallography*, 1st ed. (Eds: T. Armbruster, R. M. Danisi), De Gruyter, Berlin **2016**, p. 1.
- [20] A. Culka, J. Jehlička, *J. Raman Spectrosc.* **2019**, *50*, 262.
- [21] A. Wang, J. Han, L. Guo, J. Yu, P. Zeng, *Appl. Spectrosc.* **1994**, *48*, 959.
- [22] Wiley, Bio-Rad KnowItAll, [http://www.knowitall.com/literature/english/databases/280056-Bio-Rad\\_Raman\\_Minerals\\_HORIBA\\_Spectral\\_Database\\_Specification\\_Sheet.pdf](http://www.knowitall.com/literature/english/databases/280056-Bio-Rad_Raman_Minerals_HORIBA_Spectral_Database_Specification_Sheet.pdf)
- [23] M. Veneranda, J. Saiz, G. Lopez-reyes, J. A. Manrique, A. Sanz, C. Garcia-prieto, S. C. Werner, A. Moral, J. M. Madariaga, F. Rull, *Europlanet Science Congress*, Virtual **2020**.
- [24] J. Saiz, G. Lopez-reyes, M. Veneranda, J. A. Manrique, A. Guzmán, D. Moreno-domínguez, S. Werner, F. Poulet, J. Medina, *EGU General Assembly 2019*, Vol. 21, Vienna (Austria) **2019**, p. 17904.
- [25] C. Quantin-Nataf, J. Carter, L. Mandon, M. Balme, P. Fawdon, J. Davis, P. Thollot, E. Dehouck, L. Pan, M. Volat, C. Millot, S. Breton, D. Loizeau, J. L. Vago, *Ninth International Conference on Mars 2019*, Pasadena (California) **2019**, p. 2089.
- [26] L. Mandon, A. B. Parkes, C. Quantin-Nataf, J. C. Bridges, J. Carter, L. Pan, *Ninth International Conference on Mars 2019*, Pasadena (California) **2019**, p. 6173.
- [27] C. Quantin, J. Carter, P. Thollot, J. Broyer, L. Lozach, J. Davis, P. Grindrod, M. Pajola, E. Baratti, S. Rossato, P. Allemand, B. Bultel, C. Leyrat, J. Fernando, A. Ody, *47th Lunar and Planetary Science Conference* **2016**, p. 2863.
- [28] N. Mangold, G. Dromart, V. Ansan, F. Salese, M. G. Kleinhans, M. Massé, C. Quantin-Nataf, K. M. Stack, *Astrobiology* **2020**, *20*, 994.
- [29] J. D. Tarnas, J. F. Mustard, H. Lin, T. A. Goudge, E. S. Amador, M. S. Bramble, C. H. Kremer, X. Zhang, Y. Itoh, M. Parente, *Geophys. Res. Lett.* **2019**, *46*, 12771.
- [30] B. H. N. Horgan, R. B. Anderson, G. Dromart, E. S. Amador, M. S. Rice, *Icarus* **2020**, *339*, 113526.
- [31] D. Baratoux, M. J. Toplis, M. Monnereau, V. Sautter, *J. Geophys. Res. E Planets* **2013**, *118*, 59.
- [32] M. Grott, D. Baratoux, E. Hauber, V. Sautter, J. Mustard, O. Gasnault, S. W. Ruff, S. I. Karato, V. Debaille, M. Knapmeyer, F. Sohl, T. Van Hoolst, D. Breuer, A. Morschhauser, M. J. Toplis, *Space Sci. Rev.* **2013**, *174*, 49.
- [33] J. Carter, C. Quantin, P. Thollot, D. Loizeau, A. Ody, L. Lozach, *47th Lunar and Planetary Science Conference*, The Woodlands, Texas **2016**, 2064.
- [34] T. A. Goudge, J. F. Mustard, J. W. Head, C. I. Fassett, S. M. Wiseman, *J. Geophys. Res. Planets Res.* **2015**, *120*, 775.
- [35] J. D. Farmer, D. J. Des Marais, *J. Geophys. Res. E Planets* **1999**, *104*, 26977.
- [36] J. F. Mustard, F. Poulet, A. Gendrin, J. P. Bibring, Y. Langevin, B. Gondet, N. Mangold, G. Bellucci, F. Altieri, *Science* **2005**, *307*, 1594.
- [37] M. S. Rice, S. Gupta, A. H. Treiman, K. M. Stack, F. Calef, L. A. Edgar, J. Grotzinger, N. Lanza, L. Le Deit, J. Lasue, K. L. Siebach, A. Vasavada, R. C. Wiens, J. Williams, *J. Geophys. Res. Planets* **2017**, *122*, 2.
- [38] F. Poulet, N. Mangold, B. Platevoet, J. M. Bardintzeff, V. Sautter, J. F. Mustard, J. P. Bibring, P. Pinet, Y. Langevin, B. Gondet, A. Aléon-Toppini, *Icarus* **2009**, *201*, 84.
- [39] C. M. Pieters, R. L. Klima, T. Hiroi, M. D. Dyar, M. D. Lane, A. H. Treiman, S. K. Noble, J. M. Sunshine, J. L. Bishop, *J. Geophys. Res. E Planets* **2008**, *113*, 1.
- [40] C. A. Goodrich, *Meteorit. Planet. Sci.* **2002**, *37*, B31.
- [41] S. Hu, L. Feng, Y. T. Lin, *Chin. Sci. Bull.* **2011**, *56*, 1579.
- [42] T. Mikouchi, M. Miyamoto, *Meteorit. Planet. Sci.* **2000**, *35*, 155.
- [43] J. Carter, F. Poulet, S. Murchie, J. P. Bibring, *Planet. Space Sci.* **2013**, *76*, 53.
- [44] B. Li, J. Ge, B. Zhang, *Acta Geochim.* **2018**, *37*, 19.
- [45] J. H. Y. McSween, *Meteoritics* **1994**, *29*, 757.
- [46] C. B. Agee, D. S. Draper, *Earth Planet. Sci. Lett.* **2004**, *224*, 415.
- [47] M. R. Smith, J. L. Bandfield, *J. Geophys. Res. E Planets* **2012**, *117*, 1.
- [48] R. V. Morris, D. T. Vaniman, D. F. Blake, R. Gellert, S. J. Chipera, E. B. Rampe, D. W. Ming, S. M. Morrison, R. T. Downs, A. H. Treiman, A. S. Yen, J. P. Grotzinger, C. N. Achilles, T. F. Bristow, J. A. Crisp, D. J. D. Marais, J. D. Farmer, K. V. Fendrich, J. Frydenvang, T. G. Graff, J. M. Morookian, E. M. Stolper, S. P. Schwenzer, *Proc. Natl. Acad. Sci. U. S. A.* **2016**, *113*, 7071.
- [49] R. V. Morris, G. Klingelhöfer, B. Bernhardt, C. Schröder, D. S. Rodionov, P. A. De Souza, A. Yen, R. Gellert, E. N. Evlanov, J. Foh, E. Kankeleit, P. Gütlich, D. W. Ming, F. Renz, T. Wdowiak, S. W. Squyres, R. E. Arvidson, *Science* **2004**, *305*, 833.
- [50] R. V. Morris, G. Klingelhöfer, C. Schröder, D. S. Rodionov, A. S. Yen, D. W. Ming, J. A. de Souza, T. Wdowiak, I. Fleischer, R. Gellert, B. Bernhardt, U. Bonnes, B. A. Cohen, E. N. Evlanov, J. Foh, P. Gütlich, E. Kankeleit, T. McCoy, D. W. Mittlefehldt, F. Renz, M. E. Schmidt, B. Zubkov, S. W. Squyres, R. E. Arvidson, *J. Geophys. Res. E Planets* **2006**, *111*, E12S15.
- [51] S. Hu, Y. Li, L. Gu, X. Tang, T. Zhang, A. Yamaguchi, Y. Lin, H. Changela, *Geochim. Cosmochim. Acta* **2020**, *286*, 404.
- [52] A. H. Treiman, *Chem. Erde* **2005**, *65*, 203.
- [53] V. K. Fox, R. E. Arvidson, B. L. Jolliff, P. K. Carpenter, J. G. Catalano, M. A. G. Hinkle, R. V. Morris, *Lunar and Planetary Science Conference*, Vol. 46, The Woodlands, Texas **2015**, 2132.
- [54] B. L. Ehlmann, J. F. Mustard, C. I. Fassett, S. C. Schon, J. W. Head, D. J. Des Marais, J. A. Grant, S. L. Murchie, *Nat. Geosci.* **2008**, *1*, 355.
- [55] S. W. Ruff, *Icarus* **2004**, *168*, 131.



- [56] T. Tokano, D. L. Bish, *J. Geophys. Res. E Planets* **2005**, *110*, 1.
- [57] E. K. Gibson, D. McKay, S. J. Wentworth, R. A. Socky, *J. Chem. Inf. Model.*, **2019**, *53*, 1689.
- [58] R. V. Morris, S. W. Ruff, R. Gellert, D. W. Ming, R. E. Arvidson, B. C. Clark, D. C. Golden, K. Siebach, G. Klingelhöfer, C. Schröder, I. Fleischer, A. S. Yen, S. W. Squyres, *Science* **2010**, *329*, 421.
- [59] B. Bultel, J. C. Viennet, F. Poulet, J. Carter, S. C. Werner, *J. Geophys. Res. Planets* **2019**, *124*, 989.
- [60] A. Blanco, V. Orofino, M. D'Elia, S. Fonti, A. Mastandrea, A. Guido, F. Russo, *Icarus* **2013**, *226*, 119.
- [61] J. Flahaut, M. Massé, L. Le Deit, P. Thollot, J.-P. Bibring, F. Poulet, C. Quantin, N. Mangold, J. Michalski, J. L. Bishop, *LPI Contrib.* **2014**, *1791*, 1196.
- [62] P. R. Christensen, M. B. Wyatt, T. D. Glotch, A. D. Rogers, S. Anwar, R. E. Arvidson, J. L. Bandfield, D. L. Blaney, C. Budney, W. M. Calvin, A. Fallacaro, R. L. Fergason, N. Gorelick, T. G. Graff, V. E. Hamilton, A. G. Hayes, J. R. Johnson, A. T. Knudson, H. Y. McSween, G. L. Mehall, L. K. Mehall, J. E. Moersch, R. V. Morris, M. D. Smith, S. W. Squyres, S. W. Ruff, M. J. Wolff, *Science* **2004**, *306*, 1733.
- [63] M. Nachon, S. M. Clegg, N. Mangold, S. Schröder, L. C. Kah, G. Dromart, A. Ollila, J. R. Johnson, D. Z. Oehler, J. C. Bridges, S. Le Mouélic, O. Forni, R. C. Wiens, R. B. Anderson, D. L. Blaney, J. F. Bell III, B. Clark, A. Cousin, M. D. Dyar, B. Ehlmann, C. Fabre, O. Gasnault, J. Grotzinger, J. Lasue, E. Lewin, R. Léveillé, S. McLennan, S. Maurice, P.-Y. Meslin, W. Rapin, M. Rice, S. W. Squyres, K. Stack, D. Y. Sumner, D. Vaniman, D. Wellington, *J. Geophys. Res. Planets* **2014**, *119*, 1991.
- [64] L. C. Kah, K. M. Stack, J. L. Eigenbrode, R. A. Yingst, K. S. Edgett, *Terra Nov.* **2018**, *30*, 431.
- [65] M. Y. Zolotov, E. L. Shock, *Geophys. Res. Lett.* **2005**, *32*, 1.
- [66] G. Lopez-Reyes, F. Rull, G. Venegas, F. Westall, F. Foucher, N. Bost, A. Sanz, A. Catalá-Espí, A. Vegas, I. Hermosilla, A. Sansano, J. Medina, *Eur. J. Mineral.* **2013**, *25*, 721.
- [67] G. Lopez-Reyes, F. Rull Pérez, *J. Raman Spectrosc.* **2017**, *48*, 1654.
- [68] M. Veneranda, G. Lopez-Reyes, J. Saiz, J. A. Manrique-Martinez, A. Sanz-Arranz, J. Medina, A. Moral, L. Seoane, S. Ibarria, F. Rull, *Sci. Rep.* **2021**, *11*, 1461.
- [69] M. Veneranda, G. Lopez-Reyes, J. A. Manrique, J. Medina, P. Ruiz-Galende, I. Torre-Fdez, K. Castro, C. Lantz, F. Poulet, H. Dypvik, S. C. Werner, F. Rull, *Astrobiology* **2020**, *20*, 349.
- [70] M. Veneranda, J. A. Manrique-Martinez, G. Lopez-Reyes, J. Medina, I. Torre-Fdez, K. Castro, J. M. Madariaga, C. Lantz, F. Poulet, A. M. Krzesińska, H. Hellevang, S. C. Werner, F. Rull, *Acta - Part A Mol. Biomol. Spectrosc.* **2019**, *223*, 117360.
- [71] M. Veneranda, G. Lopez-Reyes, E. Pascual Sanchez, A. M. Krzesińska, J. A. Manrique-Martinez, A. Sanz-Arranz, C. Lantz, E. Lalla, A. Moral, J. Medina, F. Poulet, H. Dypvik, S. C. Werner, J. L. Vago, F. Rull, *Astrobiology* **2021**, *21*, 307.
- [72] M. Veneranda, G. Lopez-Reyes, J. A. Manrique-Martinez, A. Sanz-Arranz, E. Lalla, M. Konstantinidis, A. Moral, J. Medina, F. Rull, *Sci. Rep.* **2020**, *10*, 16954.
- [73] M. Veneranda, J. A. Manrique, J. Saiz, R. Navarro, J. Medina, S. Shkolyar, F. Rull, S. Maurice, R. C. Wiens, in *Lunar and Planetary Science Conference*, Virtual, **2020**, p. 1.
- [74] J. A. Manrique-Martinez, M. Veneranda, G. Lopez-Reyes, J. Saiz, J. A. Sanz, R. Navarro, J. Medina-García, F. Rull, *GeoRaman Congress 2020*, Virtual **2020**, p. 52.
- [75] A. Sanz-Arranz, J. A. Manrique-Martinez, J. Medina-García, F. Rull-Perez, *J. Raman Spectrosc.* **2017**, *48*, 1644.
- [76] N. Buzgar, U. Alexandru, I. Cuza, *ANALELE ȘTIINȚIFICE ALE Univ.* **2009**, *60*, 97.
- [77] S. Gunasekaran, G. Anbalagan, S. Pandi, *J. Raman Spectrosc.* **2006**, *37*, 892.
- [78] L. Borromeo, U. Zimmermann, S. Andò, G. Coletti, D. Bersani, D. Basso, P. Gentile, B. Schulz, E. Garzanti, *J. Raman Spectrosc.* **2017**, *48*, 983.
- [79] N. Rividi, M. Van Zuilen, P. Philippot, B. Ménez, G. Godard, E. Poidatz, *Astrobiology* **2010**, *10*, 293.
- [80] A. Sansano, G. Lopez, J. Medina, F. Rull, *Europe* **2011**, *6*, 2.
- [81] A. Steele, M. D. Fries, H. E. F. Amundsen, B. O. Mysen, M. L. Fogel, M. Schweizer, N. Z. Boctor, *Meteorit. Planet. Sci.* **2007**, *42*, 1549.
- [82] W. A. D. R. J. Reeder, *Am. Mineral* **1989**, *74*, 1159.
- [83] H. G. M. Edwards, S. E. J. Villar, J. Jehlicka, T. Munshi, *Acta - Part A Mol. Biomol. Spectrosc.* **2005**, *61*, 2273.
- [84] Y. N. Zhuravlev, V. V. Atuchin, *Nanomaterials* **2020**, *10*, 1.
- [85] S. Maurice, R. C. Wiens, P. Bernardi, P. Caïs, S. Robinson, T. Nelson, O. Gasnault, J.-M. Reess, M. Deleuze, F. Rull, J.-A. Manrique, S. Abbaki, R. B. Anderson, Y. André, S. M. Angel, G. Arana, T. Battault, P. Beck, K. Benzerara, S. Bernard, J.-P. Berthias, O. Beyssac, M. Bonafous, B. Bousquet, M. Boutillier, A. Cadu, K. Castro, F. Chapron, B. Chide, K. Clark, E. Clavé, S. Clegg, E. Cloutis, C. Collin, E. C. Cordoba, A. Cousin, J.-C. Dameury, W. D'Anna, Y. Daydou, A. Debus, L. Deflores, E. Dehouck, D. Delapp, G. De Los Santos, C. Donny, A. Doressoundiram, G. Dromart, B. Dubois, A. Dufour, M. Dupieux, M. Egan, J. Ervin, C. Fabre, A. Fau, W. Fischer, O. Forni, T. Fouchet, J. Frydenvang, S. Gauffre, M. Gauthier, V. Gharakanian, O. Gilard, I. Gontijo, R. Gonzalez, D. Granena, J. Grotzinger, R. Hassen-Khodja, M. Heim, Y. Hello, G. Hervet, O. Humeau, X. Jacob, S. Jacquino, J. R. Johnson, D. Kouach, G. Lacombe, N. Lanza, L. Lapauw, J. Laserna, J. Lasue, L. Le Deit, S. Le Mouélic, E. Le Comte, Q.-M. Lee, C. Legett, R. Leveille, E. Lewin, C. Leyrat, G. Lopez-Reyes, R. Lorenz, B. Lucero, J. M. Madariaga, S. Madsen, M. Madsen, N. Mangold, F. Manni, J.-F. Mariscal, J. Martinez-Frias, K. Mathieu, R. Mathon, K. P. McCabe, T. McConnochie, S. M. McLennan, J. Mekki, N. Melikechi, P.-Y. Meslin, Y. Mischeau, Y. Michel, J. M. Michel, D. Mimoun, A. Misra, G. Montagnac, C. Montaron, F. Montmessin, J. Moros, V. Mousset, Y. Morizet, N. Murdoch, R. T. Newell, H. Newsom, N. N. Tuong, A. M. Ollila, G. Orttner, L. Oudda, L. Pares, J. Parisot, Y. Parot, R. Pérez, D. Pheav, L. Picot, P. Pilleri, C. Pilorget, P. Pinet, G. Pont, F. Poulet, C. Quantin-Nataf, B. Quartier, D. Rambaud, W. Rapin, P. Romano, L. Roucauyrol, C. Royer, M. Ruellan, B. F. Sandoval, V. Sautter, M. J. Schoppers, S. Schröder, H.-C. Seran, S. K. Sharma, P. Sobron, M. Sodki, A. Sournac, V. Sridhar, D. Standarovsky, S. Storms, N. Striebig, M. Tatat, M. Toplis, I. Torre-Fdez, N. Toulemon, C. Velasco, M. Veneranda, D. Venhaus, C. Virmontois, M. Viso, P. Willis, K. W. Wong, *Space Sci. Rev.* **2021**, *217*, 47.

- [86] R. C. Wiens, S. Maurice, S. H. Robinson, A. E. Nelson, P. Cais, P. Bernardi, R. T. Newell, S. Clegg, S. K. Sharma, S. Storms, J. Deming, D. Beckman, A. M. Ollila, O. Gasnault, R. B. Anderson, Y. André, S. M. Angel, G. Arana, E. Auden, P. Beck, J. Becker, K. Benzerara, S. Bernard, O. Beyssac, L. Borges, B. Bousquet, K. Boyd, M. Caffrey, J. Carlson, K. Castro, J. Celis, B. Chide, K. Clark, E. Cloutis, E. C. Cordoba, A. Cousin, M. Dale, L. Deflores, D. Delapp, M. Deleuze, M. Dirmyer, C. Donny, G. Dromart, M. G. Duran, M. Egan, J. Ervin, C. Fabre, A. Fau, W. Fischer, O. Forni, T. Fouchet, R. Fresquez, J. Frydenvang, D. Gasway, I. Gontijo, J. Grotzinger, X. Jacob, S. Jacquino, J. R. Johnson, R. A. Klisiewicz, J. Lake, N. Lanza, J. Laserna, J. Lasue, S. Le Mouélic, C. Legett, R. Leveille, E. Lewin, G. Lopez-Reyes, R. Lorenz, E. Lorigny, S. P. Love, B. Lucero, J. M. Madariaga, M. Madsen, S. Madsen, N. Mangold, J. A. Manrique, J. P. Martinez, J. Martinez-Frias, K. P. McCabe, T. H. McConnochie, J. M. McGlown, S. M. McLennan, N. Melikechi, P.-Y. Meslin, J. M. Michel, D. Mimoun, A. Misra, G. Montagnac, F. Montmessin, V. Mousset, N. Murdoch, H. Newsom, L. A. Ott, Z. R. Ousnamer, L. Pares, Y. Parot, R. Pawluczyk, C. G. Peterson, P. Pilleri, P. Pinet, G. Pont, F. Poulet, C. Provost, B. Quertier, H. Quinn, W. Rapin, J.-M. Reess, A. H. Regan, A. L. Reyes-Newell, P. J. Romano, C. Royer, F. Rull, B. Sandoval, J. H. Sarrao, V. Sautter, M. J. Schoppers, S. Schröder, D. Seitz, T. Shepherd, P. Sobron, B. Dubois, V. Sridhar, M. J. Toplis, I. Torre-Fdez, I. A. Trettel, M. Underwood, A. Valdez, J. Valdez, D. Venhaus, P. Willis, *Space Sci. Rev.* **2020**, *217*, 4.
- [87] E. Boulard, F. Guyot, G. Fiquet, *Phys. Chem. Miner.* **2012**, *39*, 239.

**How to cite this article:** M. Veneranda, A. Sanz-Arranz, J. A. Manrique, J. Saiz, C. Garcia-Prieto, E. Pascual-Sánchez, J. Medina, M. Konstantinidis, E. Lalla, A. Moral, L. M. Nieto, F. Rull, G. Lopez-Reyes, *J Raman Spectrosc* **2021**, *1*. <https://doi.org/10.1002/jrs.6215>